analytical chemistry

pubs.acs.org/ac Article

On-Chip Stimulated Raman Scattering Imaging and Quantification of Molecular Diffusion in Aqueous Microfluidics

Simin Bi, Yumo Li, Jianpeng Ao, Zhijie Liu, Meilin Weng,* and Minbiao Ji*

Cite This: *Anal. Chem.* 2025, 97, 2052−2061 Read Online

ACCESS | Metrics & More | Article Recommendations | Supporting Information

ABSTRACT: Numerous chemical reactions and most life processes occur in aqueous solutions, where the physical diffusion of small molecules plays a vital role, including solvent water molecules, solute biomolecules, and ions. Conventional methods of measuring diffusion coefficients are often limited by technical complexity, large sample consumption, or significant time cost. Here, we present an optical imaging method to study molecular diffusion by combining stimulated Raman scattering (SRS) microscopy with microfluidics: a "Y"-shaped microfluidic channel forming two laminar flows with a stable concentration gradient across the interface. SRS imaging of a specific molecule allows us to obtain a high-resolution chemical profile of the diffusion region at varying inspection locations and flow rates, which enables the extraction of diffusion coefficients using the convection−diffusion model. As a proof of concept, we measured diffusion coefficients of molecules including water, protein, and multiple ions, with a sample volume of less than 1 mL and a time cost of less than 10 min. Moreover, we demonstrated a high-resolution three-dimensional (3D) reconstruction of the diffusion patterns in the microfluidic channel. The high-speed microfluidic SRS platform holds the potential for quantitative measurements of molecular diffusion, chemical reaction, and fluidic dynamics at the liquid−liquid interfaces.

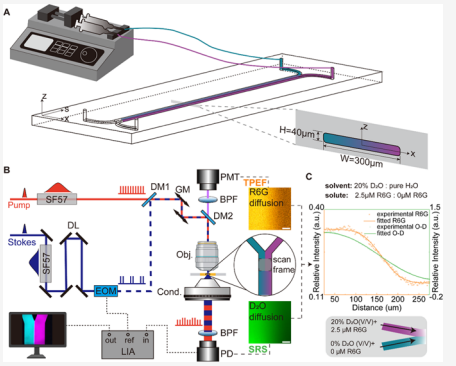

INTRODUCTION

Molecular diffusion driven by thermodynamics plays a vital role in numerous chemical[1,2] and biological[3,4] processes. For instance, water diffusion and transportation across cell memberanes[5] and blood vessels[6,7] are crucial for both basic sciences and medical research studies. As a fundamental physical quantity, diffusion coefficient (D) is critically important to many properties of fluid systems, which is closely related to molecular mass, charge, aggregation, viscosity, and so on.[8] However, obtaining accurate diffusion data is often challenging due to technical complexity, sample consumption, and time cost for conventional methods. Diaphragm cells[9,10] and interferometry[11−15] methods usually require data calibration using solutions of known diffusivity, with measurement duration spanning from hours to days. Taylor dispersion[16−20] technique offers a more convenient and rapid way to measure diffusion, but the use of long capillaries often introduces experimental errors.[21,22] Nuclear magnetic resonance (NMR)[3] is capable of measuring self-diffusion coefficients, but it has drawbacks of lower resolution, expensive equipment, and constrained substance.[23] In addition, several other optical methods using holographic interferometry,[24] phase-shifting interferometry,[25] and liquid-core cylindrical lenses[26] have been reported, but these refractive index-based methods have insufficient molecular specificity for measuring dilute solutions.

Microfluidic systems provide a promising platform for measuring diffusion coefficients using optical means. Its small dimension requires a much-reduced measurement time and sample volume.[27] Moreover, fluid stream mixing in microscale channels differs significantly from that in the macroscale.[28] Its low Reynolds number (on the order of 1) and Péclet number result in the laminar flow that is suitable for diffusion measurements.[29] Microfluidics has found widespread applications in various biochemical fields, including chemical reactions,[2] phase separation,[30−32] inertial migration investigation,[33] drug delivery,[34,35] and single-cell encapsulation.[36,37] Fluorescence detection methods have been demonstrated in combination with microfluidics for diffusion measurements.[2,38] However, they require exogenous labeling due to the lack of intrinsic molecular specificity. Hence, it is difficult to measure the diffusions of small molecules such as water and ions.

Raman scattering spectroscopy is a nondestructive vibrational spectroscopic technique showing potential for investigating diffusion processes in conjunction with microfluidics.[28,39,40] Confocal Raman microscopy has been employed to acquire Raman spectra pixel-by-pixel, enabling the measurement of lateral-resolved chemical distributions associated with diffusion. However, it suffers from slow data

Received: August 13, 2024
Revised: January 3, 2025
Accepted: January 14, 2025
Published: January 22, 2025

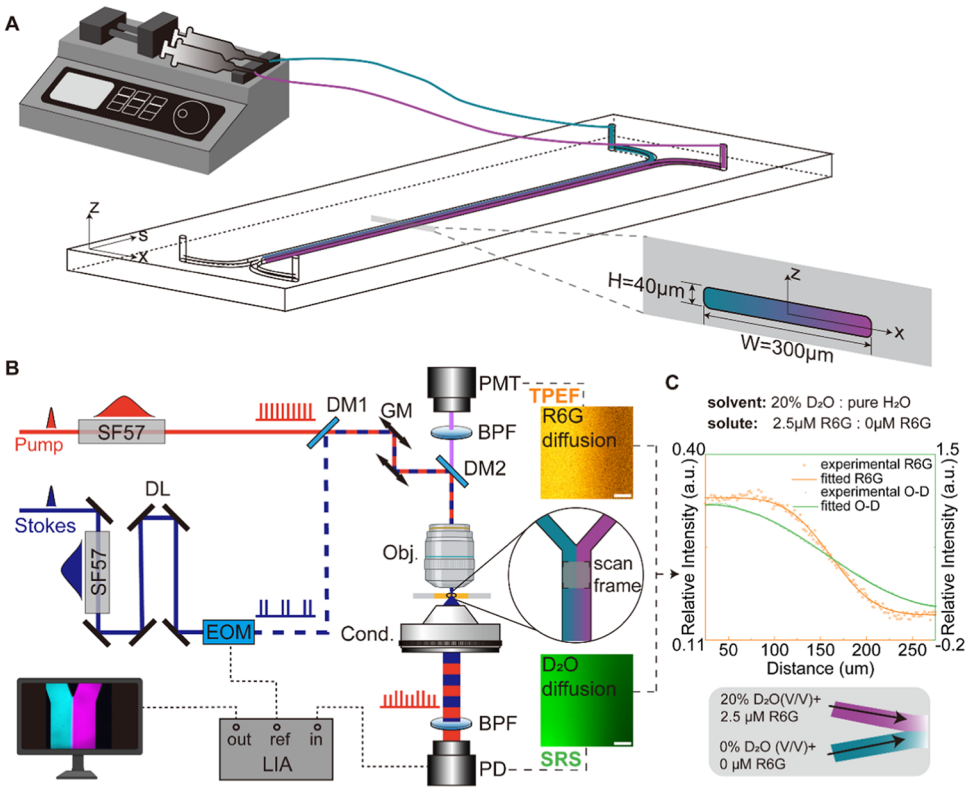

Figure 1. Experimental setup of an on-chip SRS microscope. (A) Microfluidics system including a chip with a "Y"-shaped flow channel and a dual-channel syringe pump. (B) Optical layout of the multimodal nonlinear optical microscope including SRS and TPEF for imaging the microchannels. EOM: electrooptical modulator; DM: dichroic mirror; GM: galvomirrors; PMT: photomultiplier tube; PD: photodiode; LIA: lock-in amplifier; DL: delay line; BPF: band-pass filter. Scale bars, 50 μm. (C) 1D diffusion profiles of SRS (O−D bond) for D_2O in H_2O (green) and TPEF for R6G (yellow) with a flow rate of 1 μL/min. Inset: the diagram of the concentration of solute and solvent.

acquisition speed due to weak Raman scattering cross section.[41,42] Additionally, spontaneous Raman scattering is prone to the interference of the fluorescent background from the sample or optical device. Stimulated Raman scattering (SRS) offers several orders of magnitude amplification of signal intensity with preserved spectral properties.[43] Consequently, SRS microscopy has emerged as a novel chemical imaging technique with fast speed, high sensitivity, and molecular specificity. In addition, it is capable of high-resolution three-dimensional (3D) imaging because of the nonlinear nature of signal generation.[44,45] Moreover, SRS microscopy enables convenient quantitative analysis owing to the linear dependence of signal intensity on molecular concentration.[45,46] These advantages of SRS microscopy make it a unique method for studying the diffusion of specific molecules by integrating with microfluidic platforms.

In this work, we demonstrated the effectiveness of microfluidic-compatible SRS microscopy for rapid and accurate measurement of diffusion coefficients. The technique was able to obtain spatially resolved molecular concentrations in the diffusion region at the interface between two laminar flows in the microfluidic channel. Chemical distributions could be obtained in the forms of a one-dimensional (1D) profile, two-dimensional (2D) image, and three-dimensional (3D) reconstruction. Quantification of diffusion coefficients could be extracted using a convection−diffusion model. The label-free chemical selectivity of SRS was exploited to study molecular species including water, protein, and ions. These results showed that SRS microscopy could provide a direct and rapid approach to imaging diffusion processes using microfluidic devices.

MATERIALS AND METHODS

Microfluidic System. The microfluidic setup is illustrated in Figure 1A, which consists of a double-Y-shaped microchannel enclosed between a glass substrate and a poly(dimethylsiloxane) (PDMS) layer. The glass substrate has a thickness of ∼1 mm. The PDMS is cured by heating after casting on an SU-8 mold pattern and then attaching it to the glass substrate. Flows are pushed by a dual-channel syringe pump (LSP02-2B, LongerPump, China) with 2 mL syringes. Two different liquid solutions are simultaneously injected into the two inlets of the Y-shaped entrance and converge in the main channel. The dimensions of the main channel are as follows: width (W) = 300 μm and height (H) = 40 μm (inset in Figure 1A). Volumetric flow rates are adjustable from 0.5 to 6 μL/min, resulting in a small Reynolds number (Re ∼ 1) to form laminar flow in the microchannel.

For each diffusion experiment, the microfluidic system was pre-started for ∼5 min to reach a stable laminar flow before SRS imaging. To ensure fully developed flow velocity profiles[29,47] after passing through the entrance length of the ducts, the inspection position for SRS microscopy is usually set at downstream distances more than 5000 μm away from the confluence point.

Stimulated Raman Scatter (SRS) Microscopy. The optical beam path of SRS microscopy is shown in Figure 1B. A commercial femtosecond laser system (Insight DS+, Spectra-Physics) produces two synchronized pulse trains at an 80 MHz

https://doi.org/10.1021/acs.analchem.4c04317
Anal. Chem. 2025, 97, 2052−2061

repetition rate. The fixed fundamental output of 1040 nm was employed as the Stokes beam (~200 fs), while the tunable optical parametric oscillator output (680−1300 nm, ~150 fs) served as the pump beam. To obtain sufficient spectral resolution (~20 cm^{-1}), both beams were chirped by passing through SF57 glass rods and stretched to picosecond pulses (~3.8 ps for the pump pulse and ~1.8 ps for the Stokes). The Stokes beam was modulated at 20 MHz by using an electrooptical modulator (EOM, EO-AM-R-20-C2, Thorlabs). The two laser beams were spatially and temporally overlapped via a dichroic mirror and then delivered into a laser scanning microscope (FV1200, Olympus) equipped with galvomirrors. The combined beams were focused onto the sample by a water immersion objective lens (Olympus, U XLPLN25XWMP2 25×, NA 1.05, water) with a 2 mm working distance. The transmission of the forward-going beams was collected by a high N.A. oil condenser (NA = 1.4, Nikon). After passing through a band-pass filter (CARS ET890/220, Chroma), a stimulated Raman loss (SRL) signal was detected by a reverse-biased photodiode (PD) and demodulated with a lock-in amplifier (HF2LI, Zurich Instruments) to feed the analogue input of the microscope to form SRS images. The SRS signal of the O−H stretch was recorded at the pump wavelength of 776 nm (3300 cm^{-1}), while the signal of O−D bonds was measured at the 825 nm pump (2500 cm^{-1}). In addition, the two-photon excited fluorescence (TPEF) signal could be simultaneously harvested using a band-pass filter (FF01-575/59, Semrock) and a photomultiplier tube (PMT) in the epi mode. All of the acquired images shared the same settings of 512 × 512 pixels with a pixel dwell time of 8 μs. The spatial resolution of our system is ~400 nm. To obtain large-scale two-dimensional images of the microchannel, the strip imaging method was performed by line scanning the laser spot in the width direction of the microchannel while moving the sample stage in the perpendicular (length) direction with a constant velocity of $v \sim 0.4$ μm/ms.[48] Laser powers at the microchannel were kept as pump 30 mW and Stokes 40 mW.

Sample Preparation. For water diffusion measurements, normal water and heavy water (99 atom % D, Aladdin, China) were used. For biomolecule experiments, 40 g/L bovine serum albumin (BSA) solutions were prepared by dissolving BSA powder (Fraction V, Aladdin, China) in deionized water. For ionic systems, 0.1 g/L $ZnSO_4$ aqueous solutions were prepared by dissolving $ZnSO_4 \cdot H_2O$ (99%, Aladdin, China) in deionized water; 0.5 mol/L K_2SO_4 stock solutions and 0.5 mol/L KNO_3 stock solutions were prepared to make mixed solutions of [z K_2SO_4 + (1 − z) KNO_3] with a total molar concentration of 0.25 mol/L, where z is the molar fraction of K_2SO_4.

Data Analysis. We employed the second Fick's law and the convection−diffusion model for analyzing the diffusion data in a microfluidic setup.[39] The direction of convection is defined as the s-direction (length of the microchannel), while the direction of diffusion is defined as the x-direction (width of the microchannel), and the height of the microchannel is defined as the z-axis (see Figure 1A). Several assumptions were made for our analysis. First, steady laminar flow was assumed based on the estimated small Reynolds number (Re ~ 1). Second, convection is dominated in the flow (s-) direction, while diffusion is dominated in the cross-sectional (x−z) plane due to the intermediate Péclet number (Pe = 200−4000), and the length coordinate s is proportional to contact time ($s = vt$). Third, since the channel is thin and flat ($W \gg H$), uniform concentration distribution in the z-direction is assumed despite the nonuniform velocity profile.[49] Thus, the 2D diffusion problem in the x−z plane is simplified to a quasi-1D diffusion in the x-direction, with the diffusion equation written as

$$v(x)\cdot\frac{\partial c_i(x,s)}{\partial s} = \sum_{j=1} D_{i,j}\frac{\partial^2 c_j(x,s)}{\partial x^2} \tag{1}$$

Here, $c_i(x, s)$ represents the molecular concentration of solute i, which could also represent the SRS signal intensity. Mutual diffusion coefficients of $D_{i,i}$ is the main diffusion coefficient, which represents the diffusion of solute i under its own concentration gradient, while $D_{i,j}(i \neq j)$ is the cross-diffusion coefficient, which represents the diffusion of solute i produced by the gradient in solute j. $v(x)$ represents the flow velocity distribution in the microchannel, which could be expressed analytically[47]

$$v(x) = \left(\frac{m+1}{m}\right)\left[1-\left(\frac{x}{W/2}\right)^m\right]\cdot v \tag{2}$$

where v denotes the mean velocity in the main channel and m is determined by the shape of the microchannel

$$m = 1.7 + 0.5\left(\frac{H}{W}\right)^{-1.4} \tag{3}$$

To solve the diffusion eq 1, initial conditions and boundary conditions are needed. The initial conditions are determined as

$$c_i(x,0) = \begin{cases} c_{l0,i}, & x < x_{\text{middle}} \\ c_{r0,i}, & x > x_{\text{middle}} \end{cases} \tag{4}$$

where $c_{l0,i}$ and $c_{r0,i}$ represent the initial concentrations of the two incoming left and right channels, respectively. x_{middle} denotes the confluence position of the two inlets, and boundary conditions are specified as

$$\frac{\partial c_i(0,s)}{\partial x} = \frac{\partial c_i(W,s)}{\partial x} = 0 \tag{5}$$

Fitting our measured SRS data with the above model allows the extraction of the diffusion coefficient and other parameters (x_{middle}, $c_{l0,i}$, $c_{r0,i}$, and residual norm). The optimization method adopted the Partial Differential Equation Toolbox from Matlab (MathWorks).[50]

SRS Image Processing. To eliminate imaging artifacts near the channel walls, data from the central 85% of the channel width (W = 300 μm) was used for analysis (Figure 1B). Aberrations and laser scanning result in uneven signal generation and collection in the field of view (FOV). We employed a correction method to flatten the images. First, each diffusion image was subtracted by a background image (with Stokes beam blocked). Then, a reference image was captured using a pure sample without a concentration gradient (Figure S1). The diffusion images were subsequently normalized by using the reference image to correct the unevenness caused by the optical system and device surface imperfections. In this way, calibrated SRS images were obtained for all data analysis.

RESULTS AND DISCUSSION

SRS Imaging of Water Diffusion in Microchannels with Isotope Tracing. Water diffusion is fundamentally important for many biological, chemical, and physical processes. SRS imaging at the H_2O/D_2O interface allows us

https://doi.org/10.1021/acs.analchem.4c04317
Anal. Chem. 2025, 97, 2052−2061

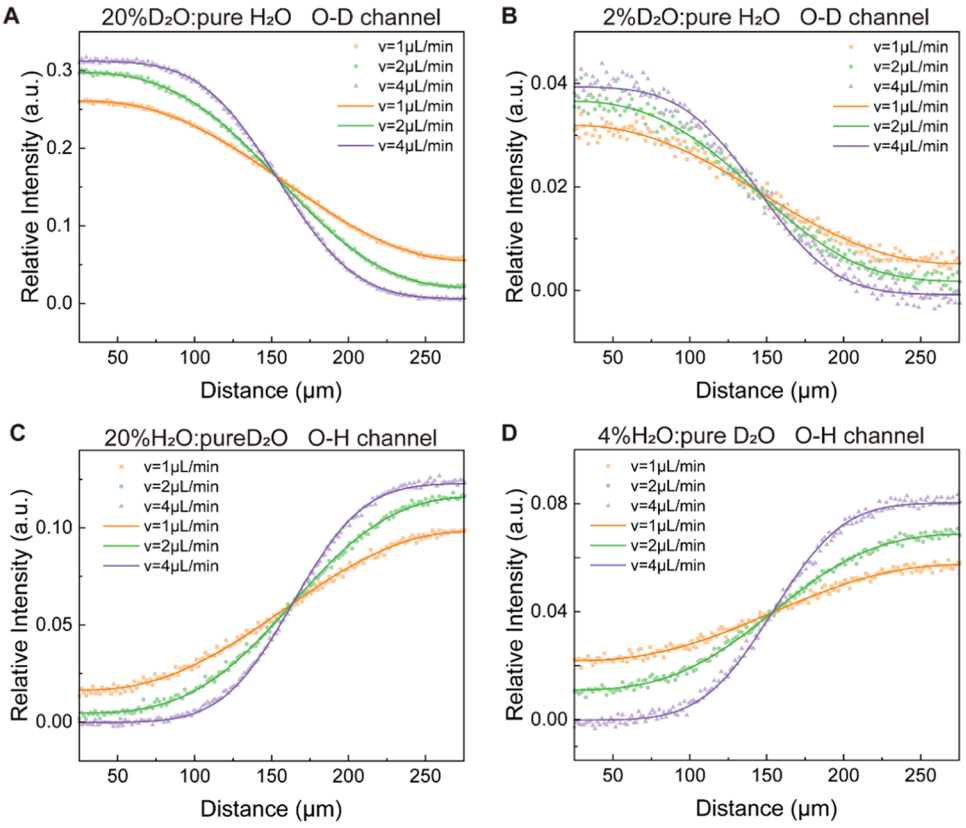

Figure 2. SRS quantification of 1D diffusion profiles of water under different concentrations and volumetric flow rates. O−D signal is measured at relatively low D_2O concentrations, with (A) 20% and (B) 2% volume fraction of D_2O/H_2O in one channel and pure H_2O in the other channel. O−H signal is measured at relatively low H_2O concentrations, with (C) 20% and (D) 4% volume fraction of H_2O/D_2O in one channel and pure D_2O in the other channel. Experimental data are shown as scattered dots, and fitting results are shown as solid lines.

to visualize the diffusion process between the two isotopologues of water. Although H_2O and D_2O exhibit many similar physical and chemical properties, such as the refractive index and density, they have distinct Raman spectral features that could be used for specific identification. While O−H stretch vibrations feature a broad Raman band over 3000−3700 cm^{-1}, the O−D stretch red-shifts the vibrational frequencies to 2200−2700 cm^{-1}.[51] SRS imaging targeted at the two well-separated Raman bands allows the quantitative mapping of H_2O and D_2O concentrations with high spatial resolution. Although fluorescent/dye molecules are often used to trace the diffusion and transportation of water, they cannot be used to measure the diffusion coefficients of water since they only represent the diffusion of fluorescent molecules rather than water itself. We demonstrated this by simultaneously measuring the diffusions of water and Rhodamine 6G with SRS and TPEF, respectively (Figure 1C, inset). Our results showed that R6G diffuses much slower than water (Figure 1C), with about 1 order of magnitude difference in diffusion coefficients (Table S1).

We first measured the SRS signal intensities of the O−D and O−H bonds and Raman spectra of D_2O/H_2O under different concentrations for calibration (Figure S2). Note that at low D_2O concentration, the HOD molecule becomes the predominant solute under chemical equilibrium. Raman spectra differ between HOD and pure D_2O because the former has a single O−D stretch mode while the latter has both symmetric and antisymmetric stretch modes. To maintain the spectral profile during diffusion, we kept the concentration difference between the two inlet channels within 20%, hence linear relationship between the deuterated molecule concentration and SRS signal could be assured in the diffusion layer. Under such conditions, a constant diffusion coefficient (D) could also be assumed, avoiding the change of D caused by large concentration variation.[26]

Figure 2 presents the measured 1D SRS intensity profiles along the diffusion direction (x-axis) at a fixed inspection position (s = 5000 μm) with varying D_2O concentrations and volumetric flow rates. Raw data and processed images are shown in Figure S3, and 1D profiles are obtained by averaging along the flow direction (s-axis) of the corresponding SRS images. We first studied the diffusion of D_2O in H_2O by imaging 20% D_2O/H_2O (volume fraction) in contact with pure H_2O (Figure 2A). It can be clearly seen that under three different flow rates (1, 2, and 4 μL/min), the concentration profile changes accordingly. A slower flow rate results in longer diffusion time and consequently reduces the concentration gradient (smoother curve). The three curves could be globally fitted by the diffusion model (eq 1), which agrees perfectly with the experimental data. The fitting results allow us to extract the mutual diffusion coefficient of HOD in H_2O (D = 2.245 × 10^{-9} m^2/s). The platform is capable of probing a much lower concentration gradient, as shown in Figure 2B, where D_2O concentration down to 2% was measurable to demonstrate the high performance of our system, with sufficient SNR enabling the accurate extraction of diffusion coefficient (D = 2.247 × 10^{-9} m^2/s). It is worth noting that measuring the SRS signal is necessary (Figure S4) of these low-

https://doi.org/10.1021/acs.analchem.4c04317
Anal. Chem. 2025, 97, 2052−2061

concentration D_2O: pure H_2O system tends to exhibit lower SNR than measuring the O−D SRS signal (Figure 2A). This is mainly caused by the fluctuation of a large O−H signal background that becomes more significant under a low concentration gradient, whereas the O−D channel has the minimum background. Similarly, H_2O diffusion in D_2O could be measured by imaging the O−H bond vibration using different volume fractions of H_2O/D_2O in contact with pure D_2O (Figure 2C,D). All of the measurement results are summarized in Table 1, with the extracted diffusion coefficients agreeing well with the literature,[11] and the standard deviations $\sigma(D)$ and root mean square errors (RMSE) are also provided. The time cost for each sample at a fixed flow rate is less than 10 min, including ∼20 s of imaging and ∼5 min to ensure steady laminar flow after a changing flow rate. The volume consumption for each sample is less than 1 mL.

Table 1. Measured Diffusion Coefficients for the Roughly/Almost Pure Normal Water (D_2O Mole Fraction N = 0.096/0.009) and Roughly/Almost Pure Heavy Water (D_2O Mole Fraction N = 0.896/0.979) from Microfluidic Experiments in This Work, along with Standard Deviation $\sigma(D)$ Obtained from Repeated Experiments in Comparison to Results from the Literature[11,a]

D_2O mole fraction N	ΔN	D (10^{-9} m^2 s^{-1})	$\sigma(D)$	RMSE	D literature (10^{-9} m^2 s^{-1})
0.096	0.096	2.235	0.006	0.18%	2.232
0.896	0.104	1.945	0.017	0.30%	1.931
0.009	0.009	2.247	0.007	0.13%	2.248
0.979	0.021	1.924	0.006	0.15%	1.922

[a]The root mean square error (RMSE) is used to describe the quality of the fitting results.

The 2D diffusion images could also be fitted using the same convection−diffusion model (eq 1) with an additional flow dimension ($s = vt$). For 20% D_2O/H_2O diffusing with pure H_2O, SRS image stripes were taken in a long range of the microchannel (S = 0−6000 μm) under the flow rates of 4 and 8 μL/min (Figure 3). The fitted images exhibit diffusion patterns that closely resemble the experimental data with low residuals. The 2D fitting result of a strip image gives $D = 2.256 \times 10^{-9}$ m^2/s for HOD diffusing in H_2O.

3D Imaging of Diffusion Profile in the Microfluidic Channel. The intrinsic optical sectioning capability of SRS microscopy was utilized to image the 3D profile of water diffusion by stepping the objective lens in the z-axis with a step size of 4 μm while taking a 2D image stripe at each depth. The depth-resolved images were rendered by utilizing the Thermo Scientific Amira software (ThermoFisher Scientific). The reconstructed volumetric image of the two water forms (D_2O in magenta and H_2O in cyan) diffusing in the microchannel could be clearly visualized (Figure 4A and Movie S1). The total time cost for taking the data in the 300 × 40 × 6000 μm^3 volume is ∼5 min. The volumetric image provides additional information compared with the 1D and 2D data. The top view (x−s-plane) shows the progressive diffusion at an increasing time (or distance). It can be seen that the D_2O solution and H_2O interface tend to be slightly shifted toward the H_2O side right after the mixing point (Figures 4B and S5). The shift of interface agrees with previous works using IR imaging.[52,53] This phenomenon could be attributed to the small differences in density and viscosity between the two streams.[29] Moreover, the depth-resolved imaging reveals that the concentration distribution along the z-direction is quite uniform, which proves the effectiveness of the quasi-1D diffusion model. Although flow velocity varies along the z-direction,[54] low aspect ratio of the channel, high diffusion coefficient, and small viscosity of the aqueous system[50] eliminate the concentration gradient in the z-direction.

Protein Diffusion in Aqueous Solution. Diffusion of biomolecules in aqueous solution is of vital importance in biological processes, occurring in tissue fluids, blood, and cell cytoplasm. In this work, we chose bovine serum albumin (BSA) for demonstration since it is a widely available and extensively studied protein in various applications.[55] Forty grams per liter BSA aqueous solutions were used in our experiments, showing that the standard Raman spectrum of protein peaked around 2930 cm^{-1}, mainly contributed by CH_3 stretching modes (Figure 5A). The linear relationship between the BSA concentration and SRS signal intensity was also verified (Figure S6A). It is worth noting that the thick poly(dimethylsiloxane) (PDMS) material used in the microchannel also exhibits a remarkable SRS background in the high-wavenumber region (Figure S6B). To extract the spectra of the BSA solution in the microchannel, background spectra using a water-filled microchannel were removed from each protein spectra, as shown in Figure 5A.

We obtained 1D diffusion profiles at various volumetric flow rates (Figure 5B). The original concentration of the BSA aqueous solution is 30 g/L in one inlet and 50 g/L in the other inlet. The diffusion curves appear steeper compared to the H_2O-D_2O system (Figure 2), indicating a slower diffusion rate of the protein molecules than water in aqueous solution. Fitting results using the convection−diffusion model are shown in Table 2. The extracted diffusion coefficient of BSA is $D = 1.61 \times 10^{-10}$ m^2/s (Table 2), similar to literature results,[56,57] demonstrating the capability of our system for measuring biomolecule diffusions.

Ion Diffusion in Aqueous Solution. Ion diffusion and transportation are fundamentally important in life science and ion batteries. In biological systems, both active ion transportation through ion channels across cell membranes and passive diffusion in the cytoplasm are essential for living cell activities. In the context of the global transition to a renewable energy economy, electrochemical storage technologies such as lithium-ion batteries play a crucial role.[58] Therefore, quantitative measurement of ion motion in electrolyte systems is essential. Traditional techniques for ion diffusion measurements, such as voltammetric restricted diffusion,[59] pulsed-field gradient spin echo,[60] and chronoamperometry[61] are time-consuming and laborious. In our microfluidic platform, we choose a 0.1 mol/L zinc sulfate ($ZnSO_4$) aqueous solution for demonstration. The Raman peak of sulfate ions (SO_4^{2-}) at around 981 cm^{-1} was used for SRS measurements. The SRS spectra of SO_4^{2-} under different concentrations are shown in Figures 6A and S7A, and calibration between the SO_4^{2-} concentration and SRS intensity is shown in Figure S7B. Akin to previous measurements, the 1D diffusion profiles at flow rates of 1, 4, and 6 μL/min (Figure 6B) were used for extracting the diffusion coefficients. Our results agree well with the literature at similar concentrations[28] (Table 3).

In addition to the simple system of a single-electrolyte aqueous solution, complex processes in multielectrolyte solution involving ternary or higher-order ion diffusions could also be studied using a microfluidic SRS platform.

https://doi.org/10.1021/acs.analchem.4c04317
Anal. Chem. 2025, 97, 2052−2061

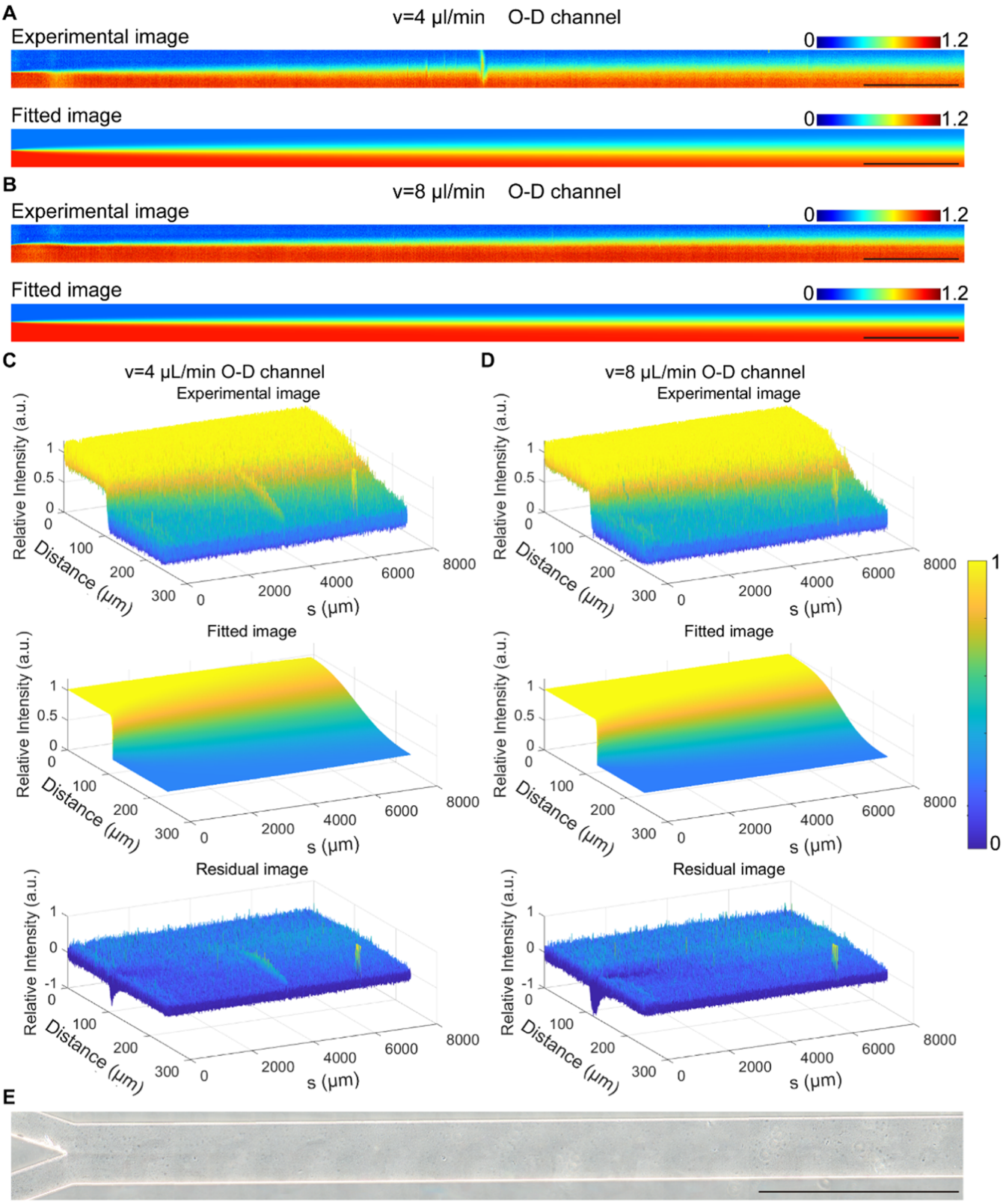

Figure 3. Imaging the diffusion of a 2% volume fraction of D_2O/H_2O into pure H_2O using SRS microscopy in the microfluidic channel. (A, B) 2D experimental and fitted images of the O−D vibrations with volumetric flow rate at 4 μL/min and 8 μL/min. (C, D) Experimental, fitted, and residual 2D maps for the two flow rates. (E) Bright-field optical image of the microchannel. Scale bars: 1000 μm.

Current methods of multicomponent diffusion measurements including optical interferometry,[62−65] diaphragm cell,[66] Taylor dispersion,[18,19,67] and conductometric method[68] only measure a single physical quantity (e.g., refractive index) for the integrated effect of all components, lacking chemical resolution for different ionic species. In contrast, SRS provides quantitative information for each ion component with a distinct Raman signature. To demonstrate such capability, we

https://doi.org/10.1021/acs.analchem.4c04317
Anal. Chem. 2025, 97, 2052−2061

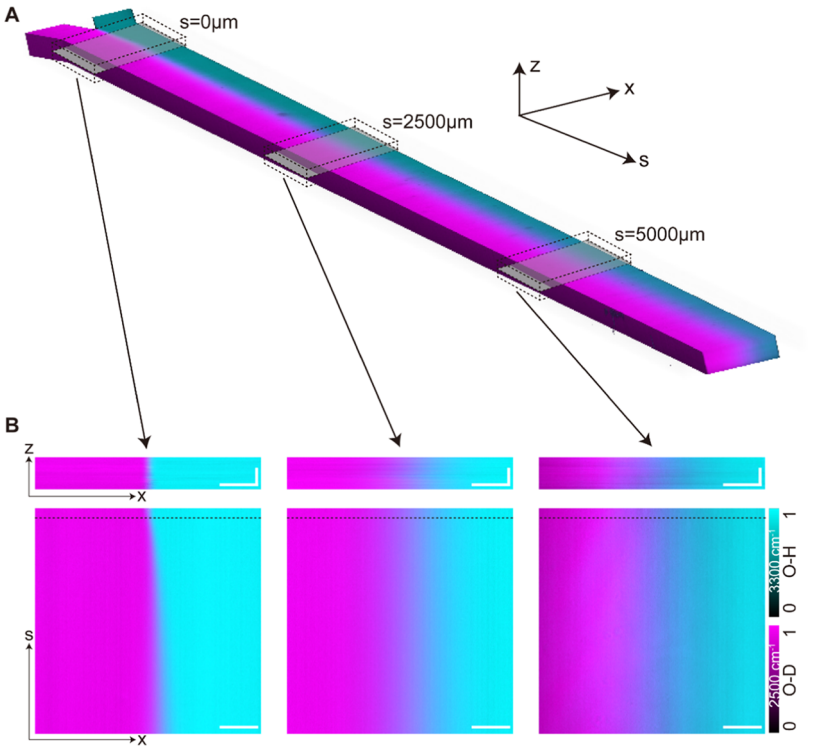

Figure 4. Volumetric SRS imaging of water diffusion in the microchannel. (A) 3D rendered view of water diffusion between pure H_2O (cyan) and pure D_2O (magenta). (B) Top view (x–s) at the depth of 20 μm of height and cross-sectional view (x–z) along the dotted line shown in the corresponding top view at three different inspection positions along the flow direction (s = 0, 2500, 5000 μm). The volumetric flow rate is 8 μL/min. Scale bars: 50 μm in x, 20 μm in z.

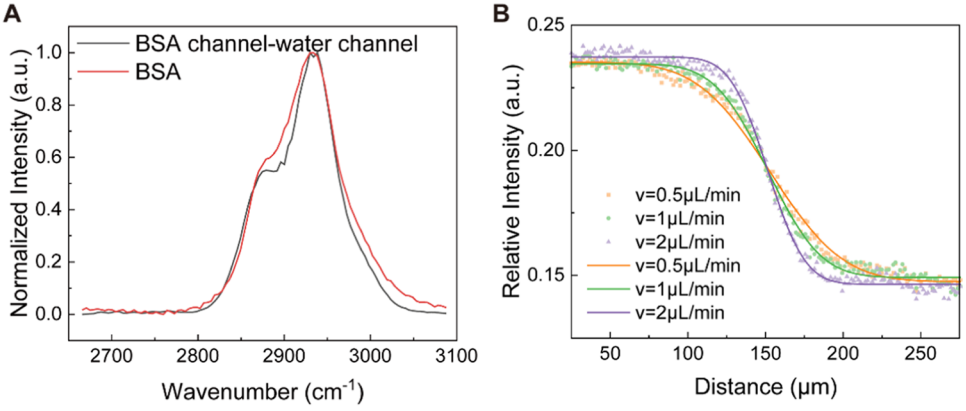

Figure 5. Measuring protein diffusion in aqueous solutions. (A) Normalized SRS spectra of standard BSA sample (black) and 40 g/L BSA solution in microchannel after background removal (red). (B) Experimental (dots) and fitted (lines) 1D profiles of the BSA diffusion at different flow rates with the 30 g/L BSA solution in one channel and the 50 g/L BSA solution in the other channel.

Table 2. Measured Diffusion Coefficient for the 40 g/L BSA Solution from Microfluidic Experiments in This Work in Comparison to the Results from the Literature[56,57,a]

BSA concentration C (g/L)	ΔC (g/L)	D (10^{-10} m^2 s^{-1})	$\sigma(D)$	RMSE	D literature (10^{-10} m^2 s^{-1})
40	20	1.61	0.022	3.7%	1.50[56]
					2.10[57]

[a]The root mean square error (RMSE) is used to describe the quality of the fitting results.

chose a ternary ionic solution of [z K_2SO_4 + (1 − z) KNO_3] with a total salt concentration of 0.25 mol/L and a molar fraction of z. In this system, the interplay between three ionic species (SO_4^{2-}, NO_3^-, K^+) makes it a complex diffusion problem to solve, including the main diffusion of SO_4^{2-} and NO_3^- (D_{11}, D_{22}) and cross-diffusion between them (D_{12}, D_{21}). The characteristic SRS spectra of SO_4^{2-} and NO_3^- (Figure 6A) offer specific detection of the diffusion profiles of the two anions simultaneously. Although a single SRS experiment can determine the diffusion coefficients within a few seconds, repeated experiments with varying molar fraction (z) and flow rates were performed for improved accuracy. The 1D diffusion profiles at z = 0.5 are shown in Figure 6C. Here, we convert the relative intensity to molarity based on the calibration results (Figure S7). Also, the measured $D_{i,j}$ under different molar fractions of z are summarized in Figure 6D.

https://doi.org/10.1021/acs.analchem.4c04317
Anal. Chem. 2025, 97, 2052−2061

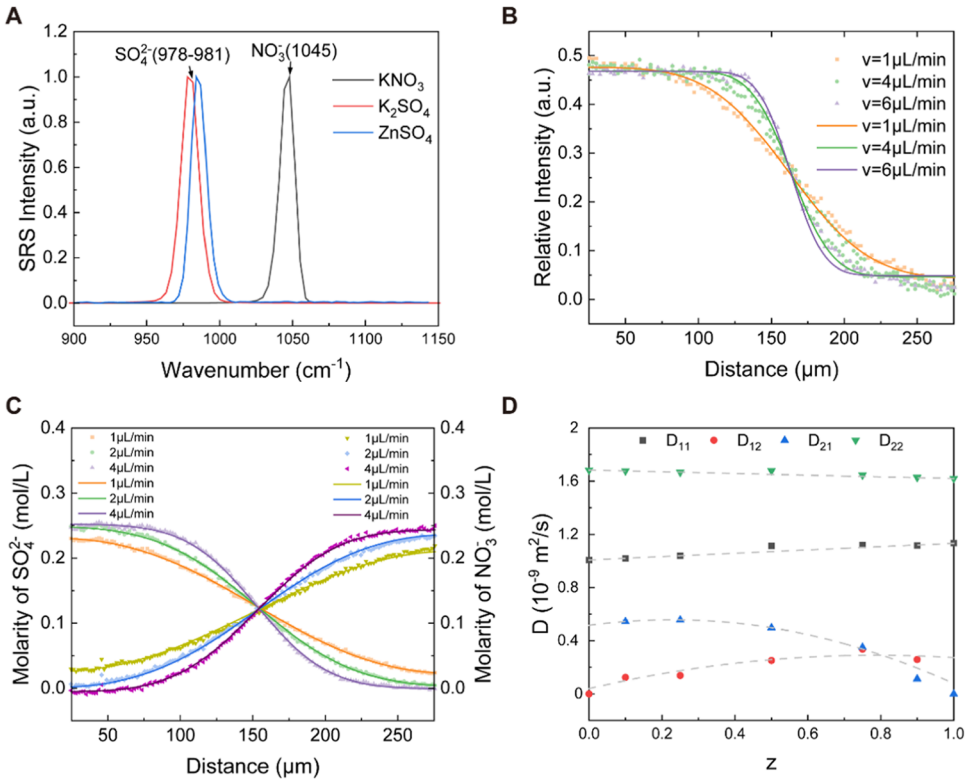

Figure 6. Ion diffusion measurements. (A) SRS spectra of SO_4^{2-} and NO_3^-. (B) Experimental (dots) and fitted (lines) 1D profiles of SO_4^{2-} diffusion at different flow rates using a 0.1 M $ZnSO_4$ solution in one channel and pure water in the other. (C) 1D diffusion profiles of $[z\ K_2SO_4 + (1 - z)\ KNO_3]$ aqueous system at molar fraction $z = 0.5$ under a total molar concentration of 0.25 mol/L. (D) Plot of the $D_{m,n}$ as a function of z under constant total molar concentration of 0.25 mol/L.

Table 3. Measured Diffusion Coefficient for the 0.1 M $ZnSO_4$ Solution from Microfluidic Experiments in This Work in Comparison to the Results from the Literature[28,a]

$ZnSO_4$ concentration C (mol/L)	ΔC (mol/L)	D (10^{-10} m^2 s^{-1})	$\sigma(D)$	RMSE	D literature (10^{-10} m^2 s^{-1})
0.1	0.1	5.76	0.05	1.2%	5.69[28]

[a]RMSE describes the quality of fitting results.

Several implications could be carefully observed from these results. First, the main diffusion coefficients of D_{11} and D_{22} are consistent with the binary diffusion coefficients of K_2SO_4[69] and KNO_3[70] as z approaches 1 and 0, respectively (at the same concentration of 0.25 mol/). On the other hand, D_{11} approximates the tracer diffusion coefficient of SO_4^{2-} in 0.25 mol/L KNO_3 solution as z approaches 0,[71,72] whereas D_{22} approximates the tracer diffusion coefficient of NO_3^- in the supporting K_2SO_4 solution of the same concentration as z approaches 1.[73] Moreover, it can be easily understood that the cross-diffusion coefficients of D_{12} and D_{21} approach 0 as z approaches 0 and 1, respectively. The measured positive D_{12} and D_{21} reveal complex interactions between different ionic species. At 25 °C, the limiting ionic diffusion coefficients can be theoretically calculated from the Nernst−Einstein formula: $D_0(SO_4^{2-}) = 1.065 \times 10^{-9}$ m^2/s, $D_0(NO_3^-) = 1.902 \times 10^{-9}$ m^2/s, $D_0(K^+) = 1.957 \times 10^{-9}$ m^2/s.[67] The limiting ionic diffusion coefficient of K^+ is larger than that of SO_4^{2-}, thus an internal electric field[67] could be generated due to the concentration gradient of K_2SO_4, which slows down K^+ and speeds up SO_4^{2-}. If the NO_3^- ion is present, the internal electric field will also increase the motion of NO_3^- in the same direction as the K_2SO_4 gradient, resulting in positive D_{21}. D_{12} is also positive in a similar way.

The microfluidic SRS system could be extended to study various physical and chemical processes in the liquid phase, such as chemical reactions at the liquid−liquid interface and fluid dynamics associated with mixed molecular compositions. Chemical reaction kinetics may be visualized if the reactant and product molecules have distinct Raman spectral signatures. Other nonlinear optical imaging modalities could also be included to add detection channels for nanoparticles and fluorescence molecules, such as transient absorption,[74] two-photon excited fluorescence, etc. Interface-specific measurements may be performed by second harmonic generation (SHG) microscopy to study molecular assembly and ordering at the flow interface with polarization control. Solutions exhibiting tunable surface tensions with variable chemical compositions may provide a model system for studying interesting fluid dynamics under critical conditions using the microfluid-SRS setup.[30,33] Furthermore, the 3D imaging capability of SRS can be critical for fluid systems that may yield curved interfaces and significant vertical concentration gradients.

CONCLUSIONS

In summary, we have demonstrated an efficient platform for measuring the diffusion coefficients of various types of

https://doi.org/10.1021/acs.analchem.4c04317
Anal. Chem. 2025, 97, 2052−2061

molecules by integrating microfluidics with SRS microscopy. The system allows unique high-spatiotemporal-resolution measurements of molecular concentration with chemical specificity, generating data in multiple dimensions including 1D diffusion profiles, 2D chemical images, and 3D reconstructions of the diffusion pattern. The reduced experimental duration and sample consumption are practically advantageous to cope with precious specimens. Our method holds potential for on-chip studies for a broad range of research at the liquid−liquid interface without exogenous labeling.

■ ASSOCIATED CONTENT

Supporting Information

The Supporting Information is available free of charge at https://pubs.acs.org/doi/10.1021/acs.analchem.4c04317.

Movie S1 (MPG)

Image processing diagram for the H_2O−D_2O system (Figure S1); the spontaneous Raman (SR) and stimulated Raman scattering (SRS) spectrum of D_2O/H_2O under different concentrations and the relationship between SRS signal intensity and the concentration of D_2O/H_2O (Figure S2); the original and processed images captured by a SRS microscope of water diffusion in microchannels (Figure S3); 1D diffusion profiles of water diffusion in microchannels (Figure S4); top views (x−s) at the depth of 20 μm of height of the microchannel and cross-sectional views (x−z) of water diffusion systems in microchannels (Figure S5); the SRS spectrum of the BSA solution and PDMS channel and the linear relationship between SRS signal intensity and the BSA concentration (Figure S6); and the linear relationship between the concentration of SO_4^{2-} and NO_3^- and their SRS signal intensity (Figure S7) (PDF)

■ AUTHOR INFORMATION

Corresponding Authors

Meilin Weng − *Department of Anesthesiology, Zhongshan Hospital, Fudan University, Shanghai 200032, China*; Email: 15111230032@fudan.edu.cn

Minbiao Ji − *State Key Laboratory of Surface Physics and Department of Physics, Academy for Engineering and Technology, Key Laboratory of Micro and Nano Photonic Structures (Ministry of Education), Shanghai Key Laboratory of Metasurfaces for Light Manipulation, Fudan University, Shanghai 200433, China*; orcid.org/0000-0002-9066-4008; Email: minbiaoj@fudan.edu.cn

Authors

Simin Bi − *State Key Laboratory of Surface Physics and Department of Physics, Academy for Engineering and Technology, Key Laboratory of Micro and Nano Photonic Structures (Ministry of Education), Shanghai Key Laboratory of Metasurfaces for Light Manipulation, Fudan University, Shanghai 200433, China*

Yumo Li − *State Key Laboratory of Surface Physics and Department of Physics, Academy for Engineering and Technology, Key Laboratory of Micro and Nano Photonic Structures (Ministry of Education), Shanghai Key Laboratory of Metasurfaces for Light Manipulation, Fudan University, Shanghai 200433, China*

Jianpeng Ao − *State Key Laboratory of Surface Physics and Department of Physics, Academy for Engineering and Technology, Key Laboratory of Micro and Nano Photonic Structures (Ministry of Education), Shanghai Key Laboratory of Metasurfaces for Light Manipulation, Fudan University, Shanghai 200433, China*

Zhijie Liu − *State Key Laboratory of Surface Physics and Department of Physics, Academy for Engineering and Technology, Key Laboratory of Micro and Nano Photonic Structures (Ministry of Education), Shanghai Key Laboratory of Metasurfaces for Light Manipulation, Fudan University, Shanghai 200433, China*

Complete contact information is available at: https://pubs.acs.org/10.1021/acs.analchem.4c04317

Author Contributions

M.B.J. and M.L.W. conceived the work. S.M.B. and Y.M.L. performed SRS measurements and data analysis. J.P.A. and Z.J.L. helped with experiments. S.M.B. and M.B.J. wrote the manuscript, and all authors reviewed and approved it.

Notes

The authors declare no competing financial interest.

■ ACKNOWLEDGMENTS

The authors acknowledge the financial support from the National Key R&D Program of China (2021YFF0502900), the National Natural Science Foundation of China (62425501 and 82372502), the Municipal Natural Science Foundation of Shanghai (23dz2260100), and the Shanghai Medical Innovation Research Special Funding (23Y11902300).

■ REFERENCES

(1) Abonnenc, M.; Josserand, J.; Girault, H. H. *Lab Chip* **2009**, *9* (3), 440−448.
(2) Qiu, J.; Bao, B.; Zhao, S.; Lu, X. *Chem. Eng. Sci.* **2021**, *231*, No. 116248.
(3) Burstein, D.; Gray, M. L.; Hartman, A. L.; Gipe, R.; Foy, B. D. *J. Orthop. Res.* **1993**, *11* (4), 465−478.
(4) Chiu, W. S.; Belsey, N. A.; Garrett, N. L.; Moger, J.; Delgado-Charro, M. B.; Guy, R. H. *Proc. Natl. Acad. Sci. U.S.A.* **2015**, *112* (25), 7725−7730.
(5) Potma, E. O.; De Boeij, W. P.; Van Haastert, P. J. M.; Wiersma, D. A. *Proc. Natl. Acad. Sci. U.S.A.* **2001**, *98* (4), 1577−1582.
(6) Lucotte, B. M.; Powell, C.; Knutson, J. R.; Combs, C. A.; Malide, D.; Yu, Z.-X.; Knepper, M.; Patel, K. D.; Pielach, A.; Johnson, E.; et al. *Proc. Natl. Acad. Sci. U.S.A.* **2017**, *114* (18), 4805−4810.
(7) Egawa, G.; Ono, S.; Kabashima, K. Intravital Imaging of Vascular Permeability by Two-Photon Microscopy. In *Animal Models of Allergic Disease: Methods and Protocols*; Nagamoto-Combs, K., Ed.; Springer US: New York, NY, 2021; pp 151−157.
(8) Evans, R.; Dal Poggetto, G.; Nilsson, M.; Morris, G. A. *Anal. Chem.* **2018**, *90* (6), 3987−3994.
(9) Stokes, R. H. *J. Am. Chem. Soc.* **1950**, *72* (2), 763−767.
(10) Easteal, A. J.; Price, W. E.; Woolf, L. A. *J. Chem. Soc., Faraday Trans. 1* **1989**, *85* (5), 1091.
(11) Longsworth, L. G. *J. Phys. Chem. A* **1960**, *64*, 1914−1917, DOI: 10.1021/j100841a027.
(12) Miller, D. G. *J. Solution Chem.* **2014**, *43* (1), 6−25.
(13) Creeth, J. M. *J. Am. Chem. Soc.* **1955**, *77* (24), 6428−6440.
(14) Miller, D. G.; Albright, J. G.; Mathew, R.; Lee, C. M.; Rard, J. A.; Eppstein, L. B. *J. Phys. Chem. A* **1993**, *97*, 3885−3899.
(15) Miller, D. G.; Paduano, L.; Sartorio, R.; Albright, J. G. *J. Phys. Chem. A* **1994**, *98* (51), 13745−13754.
(16) Chen, L.; Leaist, D. G. *J. Solution Chem.* **2014**, *43* (12), 2224−2237.

(17) Taylor, G. *Proc. R. Soc. London, Ser. A* **1953**, *219* (1137), 186−203.
(18) Leaist, D. G.; Hao, L. *J. Solution Chem.* **1993**, *22* (3), 263−277.
(19) Leaist, D. G. *Ber. Bunsenges. Phys. Chem.* **1991**, *95* (2), 117−122.
(20) Otzen, D. E.; Buell, A. K.; Jensen, H. *Curr. Opin. Struct. Biol.* **2021**, *70*, 8−15.
(21) Van de Ven-Lucassen, I. M. J. J.; Kieviet, F. F.; Kerkhof, P. P. *J. Chem. Eng. Data* **1995**, *40*, 407−411.
(22) Haghi, A. *Research Methodologies in Applied Chemistry with Multidisciplinary Perspectives*, 2021.
(23) Murday, J. S.; Cotts, R. M. *J. Chem. Phys.* **1970**, *53* (12), 4724−4725.
(24) Gomes, D. C.; Geraldes, V.; Fegley, D.; Rodrigues, M. A. *Chem. Eng. Sci.* **2021**, *236*, 116478.
(25) Komiya, A.; Maruyama, S. *Exp. Therm. Fluid Sci.* **2006**, *30* (6), 535−543.
(26) Meng, W.; Xia, Y.; Chen, Y.; Pu, X. *Sci. Rep.* **2018**, *8* (1), No. 12610, DOI: 10.1038/s41598-018-30650-z.
(27) Whitesides, G. M. *Nature* **2006**, *442* (7101), 368−373.
(28) Chen, B.; Xuan, J.; Offer, G. J.; Wang, H. *Appl. Energy* **2020**, *279*, No. 115687.
(29) Watkin, S. A. J.; Bennie, R. Z.; Gilkes, J. M.; Nock, V. M.; Pearce, F. G.; Dobson, R. C. J. *Eur. Biophys. J.* **2023**, *52* (4−5), 459−471.
(30) Huh, Y. S.; Jeong, C.-M.; Chang, H. N.; Lee, S. Y.; Hong, W. H.; Park, T. J. *Biomicrofluidics* **2010**, *4* (1), No. 014103.
(31) Lu, Y.; Xia, Y.; Luo, G. *Microfluid. Nanofluid.* **2011**, *10* (5), 1079−1086.
(32) Meagher, R. J.; Light, Y. K.; Singh, A. K. *Lab Chip* **2008**, *8* (4), 527−532.
(33) Guan, G.; Wu, L.; Bhagat, A. A.; Li, Z.; Chen, P. C. Y.; Chao, S.; Ong, C. J.; Han, J. *Sci. Rep.* **2013**, *3* (1), No. 1475, DOI: 10.1038/srep01475.
(34) Kobayashi, H.; Lei, C.; Wu, Y.; Mao, A.; Jiang, Y.; Guo, B.; Ozeki, Y.; Goda, K. *Sci. Rep.* **2017**, *7* (1), No. 12454, DOI: 10.1038/s41598-017-12378-4.
(35) Neužil, P.; Giselbrecht, S.; Lange, K.; Huang, T. J.; Manz, A. *Nat. Rev. Drug Discovery* **2012**, *11* (8), 620−632.
(36) Brouzes, E.; Medkova, M.; Savenelli, N.; Marran, D.; Twardowski, M.; Hutchison, J. B.; Rothberg, J. M.; Link, D. R.; Perrimon, N.; Samuels, M. L. *Proc. Natl. Acad. Sci. U.S.A.* **2009**, *106* (34), 14195−14200.
(37) Choi, D.; Lee, E.; Kim, S.-J.; Han, M. *Soft Matter* **2019**, *15* (23), 4647−4655.
(38) Ismagilov, R. F.; Stroock, A. D.; Kenis, P. J. A.; Whitesides, G.; Stone, H. A. *Appl. Phys. Lett.* **2000**, *76* (17), 2376−2378.
(39) Peters, C.; Wolff, L.; Haase, S.; Thien, J.; Brands, T.; Koß, H.-J.; Bardow, A. *Lab Chip* **2017**, *17* (16), 2768−2776.
(40) Forster, J. D.; Harris, S. J.; Urban, J. J. *J. Phys. Chem. Lett.* **2014**, *5* (11), 2007−2011.
(41) Huang, W. E.; Griffiths, R. I.; Thompson, I. P.; Bailey, M. J.; Whiteley, A. S. *Anal. Chem.* **2004**, *76* (15), 4452−4458.
(42) Van Manen, H.-J.; Lenferink, A.; Otto, C. *Anal. Chem.* **2008**, *80* (24), 9576−9582.
(43) Freudiger, C. W.; Min, W.; Saar, B. G.; Lu, S.; Holtom, G. R.; He, C.; Tsai, J. C.; Kang, J. X.; Xie, X. S. *Science* **2008**, *322* (5909), 1857−1861.
(44) Ao, J.; Feng, Y.; Wu, S.; Wang, T.; Ling, J.; Zhang, L.; Ji, M. *Small Methods* **2020**, *4* (2), No. 1900600, DOI: 10.1002/smtd.201900600.
(45) Chen, X.; Zhang, C.; Lin, P.; Huang, K. C.; Liang, J.; Tian, J.; Cheng, J. X. *Nat. Commun.* **2017**, *8*, No. 15117.
(46) Fu, D.; Lu, F.-K.; Zhang, X.; Freudiger, C.; Pernik, D. R.; Holtom, G.; Xie, X. S. *J. Am. Chem. Soc.* **2012**, *134* (8), 3623−3626.
(47) Rohsenow, W. M.; Hartnett, J. P.; Cho, Y. I. *Handbook of Heat Transfer*; McGraw-Hill Professional, 1998.
(48) Zhang, B.; Sun, M.; Yang, Y.; Chen, L.; Zou, X.; Yang, T.; Hua, Y.; Ji, M. *Biomed. Opt. Express* **2018**, *9* (6), 2604−2613.
(49) Kamholz, A. E.; Weigl, B. H.; Finlayson, B. A.; Yager, P. *Anal. Chem.* **1999**, *71* (23), 5340−5347.
(50) Häusler, E.; Domagalski, P.; Ottens, M.; Bardow, A. *Chem. Eng. Sci.* **2012**, *72*, 45−50.
(51) Gorelik, V. S.; Avakyants, L. P.; Skrabatun, A. V. *J. Raman Spectrosc.* **2022**, *53* (1), 128−136.
(52) Chevalier, S.; Tourvieille, J. N.; Sommier, A.; Pradère, C. *Chem. Eng. J. Adv.* **2021**, *8*, 100166.
(53) Carandang, G. G.; Nakanishi, R.; Kakuta, N. *Chem. Eng. J.* **2024**, *479*, 147697.
(54) Song, H.; Bringer, M. R.; Tice, J. D.; Gerdts, C. J.; Ismagilov, R. F. *Appl. Phys. Lett.* **2003**, *83* (12), 4664−4666.
(55) Gaigalas, A. K.; Hubbard, J. B.; McCurley, M.; Woo, S. *J. Phys. Chem. A* **1992**, *96* (5), 2355−2359.
(56) Barish, A. O.; Gabriel, D. A.; Johnson, C. S. *J. Chem. Phys.* **1987**, *87* (6), 3594−3602.
(57) Weissmana, M. B.; Pan, R. C.; Wareb, B. R. *J. Chem. Phys.* **1979**, *70* (6), 2897−2903.
(58) Khaligh, A.; Zhihao, L. *IEEE Trans. Veh. Technol.* **2010**, *59* (6), 2806−2814.
(59) Hou, T.; Monroe, C. W. *Electrochim. Acta* **2020**, *332*, 135085.
(60) Saito, Y.; Yamamoto, H.; Nakamura, O.; Kageyama, H.; Ishikawa, H.; Miyoshi, T.; Matsuoka, M. *J. Power Sources* **1999**, *81*, 772−776, DOI: 10.1016/s0378-7753(99)00101-9.
(61) Saw, E. N.; Blanc, N.; Kanokkanchana, K.; Tschulik, K. *Electrochim. Acta* **2018**, *282*, 317−323.
(62) Rard, J. A.; Albright, J. G.; Miller, D. G.; Zeidle, M. E. *J. Chem. Soc., Faraday Trans.* **1996**, *92*, 4187−4197.
(63) Albright, J. G.; Gillespie, S. M.; Rard, J. A.; Miller, D. G. *J. Chem. Eng. Data* **1998**, *43* (4), 668−675, DOI: 10.1021/je9800196.
(64) Annunziata, O.; Rard, J. A.; Albright, J. G.; Paduano, L.; Miller, D. G. *J. Chem. Eng. Data* **2000**, *45* (5), 936−945.
(65) Annunziata, O.; Miller, D. G.; Albright, J. G. *J. Mol. Liq.* **2010**, *156* (1), 33−37.
(66) Spallek, M.; Hertz, H. G.; Funsch, M.; Herrmann, H.; Weingärtner, H. *Ber. Bunsenges. Phys. Chem.* **1990**, *94* (3), 365−376.
(67) Deng, Z.; Leaist, D. G. *Can. J. Chem.* **1991**, *69* (10), 1548−1553, DOI: 10.1139/v91-229.
(68) Leaist, D. G. *Electrochim. Acta* **1988**, *33* (6), 795−799.
(69) Rard, J. A.; Miller, D. G.; Albright, J. G.; Zeidler, M. E.; Annunziata, O. *J. Solution Chem.* **2021**, *50* (11−12), 1315−1334.
(70) Daniel, V.; Albright, J. G. *J. Solution Chem.* **1991**, *20* (6), 633−642.
(71) Tanaka, K. *J. Chem. Soc., Faraday Trans. 1* **1988**, *84* (8), 2895−2897.
(72) Applin, K. R.; Lasaga, A. C. *Geochim. Cosmochim. Acta* **1984**, *48* (10), 2151−2162.
(73) Hashitani, T.; Tanaka, K. *J. Chem. Soc., Faraday Trans. 1* **1983**, *79* (8), 1765−1768.
(74) Zhang, L.; Shen, S.; Liu, Z.; Ji, M. *Adv. Biosyst.* **2017**, *1* (4), No. 1700013, DOI: 10.1002/adbi.201700013.

https://doi.org/10.1021/acs.analchem.4c04317
Anal. Chem. 2025, 97, 2052−2061